MDPI

Article

Formation Mechanisms and Crack Propagation Behaviors of White Etching Layers and Brown Etching Layers on Raceways of Failure Bearings

Xiaochen Zhang [1,2], Di Wu [1,3,*], Yaming Zhang [2], Lijia Xu [4], Jianqiu Wang [1,2,5,*] and En-Hou Han [1,2,5]

[1]   School of Materials Science and Engineering, University of Science and Technology of China, 72 Wenhua Road, Shenyang 110016, China
[2]   CAS Key Laboratory of Nuclear Materials and Safety Assessment, Institute of Metal Research, Chinese Academy of Sciences, 62 Wencui Road, Shenyang 110016, China
[3]   Shi-Changxu Innovation Center for Advanced Materials, Institute of Metal Research, Chinese Academy of Sciences, 72 Wenhua Road, Shenyang 110016, China
[4]   Manufacturing Department of Bayuquan Iron & Steel Subsidiary, Angang Steel Company Ltd., Yingkou 115007, China
[5]   Institute of Corrosion Science and Technology, 136 Kaiyuan Avenue, Guangzhou 510530, China
*   Correspondence: dwu@imr.ac.cn (D.W.); wangjianqiu@imr.ac.cn (J.W.)

Abstract: White etching layers (WELs) and brown etching layers (BELs), formed on the upper layer of bearing raceways generally lead to surface crack initiation and propagation and significantly affect the stable operation of precision bearings. In this study, the microstructure features of WELs and BELs from two failure bearings have been characterized and analyzed. The BEL mainly consists of quenched martensite with higher hardness values. The bainite simultaneously exists at the boundary of the BEL/matrix. Owing to the relative roll and slip, temperature increases and rapid decreases are the main formation mechanisms of the BEL in this study (thermal-induced effect). The WEL can be only found on one sample, and elongated and coarse grains are found in this region. It can be speculated that the WEL may originate from the surface region temperature increasing again and then slowly decreasing. Cracks can initiate at the boundaries of the WEL/BEL/matrix. The crack propagation behaviors are significantly affected by the properties of the WEL and BEL microstructure. It is difficult for the cracks to propagate from a softer WEL into a harder BEL. Thus, the depth of cracks in the WEL is shallower. However, because of the brittle nature of quenched martensite in the BEL, cracks can easily propagate downward under contact stress. Thus, the depth of cracks can exceed 100 μm easily. The formation mechanisms of the WEL/BEL and crack propagation behaviors have been further proved and discussed in this study.

Keywords: white etching layer (WEL); brown etching layer (BEL); thermal-induced effect; crack propagation behavior; martensite-bearing raceways

1. Introduction

White etching layers (WELs) and brown etching layers (BELs) are one of the typical damage modes of rolling contact fatigue (RCF) existing on surfaces of rail or bearing raceways after subjecting numerous contact cycles. The WEL and BEL are usually located on the upper layers of the contact surface and are named from their white and brown color characteristics observed by an optical microscope.

The microstructure features of the WEL and BEL are characterized in many studies. Most of these studies are concentrated on pearlite railways. Generally, the WEL mainly consists of ultra-fine martensite [1–3], fine grains of ferrite [2,4] or severe plastic deformation pearlite [5], and some retained austenite. Li [6] pointed out that the BEL may be a new microstructure on rail surfaces under real working conditions, and the features and

formation of the BEL have not been studied clearly. The BEL mainly consists of martensite [6,7], austenite and primary cementite laths [7], and bainitic [8]. For martensite-bearing raceways, the WEL mainly consists of refined martensite grains [9], tempered microstructures [10], or austenite with coarse grains [11]. The BEL mainly consists of quenched martensite with higher hardness values [11]. The main phases in the WEL and BEL are significantly different.

Though many studies have reported this damage mode and analyzed relevant formation mechanisms, in the latest report [12], an alternating ". . .WEL–BEL–WEL–BEL–WEL–BEL. . ." sandwich structure was found on bainite railway. Even so, there is still no unified formation mechanism that can be widely accepted. The accepted formation mechanisms of the WEL and BEL are stress-induced effect [7,13–15], thermal-induced effect [16–18], or the interaction of the two effects [9]. However, these explanations are responsible for their characteristic results. There is no simple mechanism that can explain all of these cases. When the microstructure in near-surface regions (usually less than hundreds of microns from surfaces) plastically deforms under the cyclic contact stress, lots of heat can be generated accumulatively on surfaces. Thus, univariate experiments are necessary. By applying surface laser treatment, Guzman and Su [10,19] studied the formation of the WEL, which does not seem to simultaneously realize the occurrence of the WEL and BEL. Pena [20] proved that the white etching structure is related to the severe plastic deformation conditions by high-pressure torsion tests. Similarly, no brown etching structure can be found in this study. Qin [21] pointed out that cementite decomposition can occur by high-pressure torsion conditions, which also proved that element migration or phase transformation can be realized by severe plastic deformation. The diffusion of carbon and other alloying elements can significantly affect the properties of steel [22–25]. Rare references reported that the BEL can be found under the WEL structure in univariate experiments. However, the WEL and BEL can appear simultaneously on railway surfaces operating under real working conditions [6–8,26], which indicates that the formation of the two layers may be associated with the complex interaction of the two effects. In material processing, especially in hard-cutting processing, the white layer and dark layer are distributed on the upper layer of the surface. Zhang [27] also proved that this sandwich construction (white layer/dark layer/matrix) results from the complex interaction of the stress-induced and thermal-induced effects.

Due to the different mechanical properties between the WEL/BEL/matrix, the cracks can initiate from the surface and propagate along the boundaries, leading to squats on railways [28,29] or peeling bands on the bearing raceways [11]. Though residual compressive stresses usually can be detected on rolling surfaces [30–32], there seems to be no close relationship between the crack propagation behaviors in the WEL/BEL and residual stress. Mechanical behaviors and microstructure features usually become more important. Ostash [33] studied micropits and spalls on surfaces of railroad wheels and pointed out the characteristics of cyclic crack resistance of steel under the conditions of mode I and mode II fracture. Ren [34] also pointed out that the RCF cracks can be accurately predicted and combined with the superposition of fracture mode I + II + III. Kumar's results [7] show that cracks initiate on the surface, propagate along the boundary of the WEL and BEL, and ultimately propagate into the matrix. However, Su [19] pointed out that cracks can initiate in the quenching area (white etching area) rather than the boundaries of the quenching area and the matrix. Mojumder [4] also proved that cracks originate from the brittle WEL region, and crack propagation is driven by bending stresses. Seo [35] found two types of cracks in RCF test specimens: one type of crack initiates at the boundaries of the WEL and the matrix, while the other type of crack initiates at the center of the WEL. Carroll [36] studied the crack morphologies in detail, and the propagation behaviors should be associated with the plastic deformation of pearlite. The cracks stop propagating into the matrix when the plastic deformation exists at the boundaries of the WEL and the matrix.

The microstructure and the crack propagation behaviors of the WEL/BEL from pearlite railway surfaces have been widely investigated. But the WEL and BEL formed on

martensite-bearing raceways under real working conditions have not been studied clearly, and the related references are insufficient. There is a significant difference between rails of steel and bearings of steel in the aspect of crack initiation and propagation behaviors. Thus, it is necessary to study the features of the WEL/BEL formed under real working conditions. In this study, two bearings operating under real working conditions until complete failure were dissected and analyzed. The WEL and BEL on the raceway surfaces of two bearings can be found. The features of the WEL and BEL have been microscopically characterized by multiple methods. Then, the formation mechanisms of the WEL and BEL have been analyzed, and the surface crack initiation and propagation behaviors have been summarized. This study aims at the further acknowledgment of features of the microstructure and crack propagation behaviors of the WEL/BEL on martensite-bearing raceways.

2. Experimental Procedure

Two bearing samples were taken from factories. The samples operated under real working conditions until complete failure. The failure criterion of the two bearings was increasing vibration, which exceeds the limited vibration value. Sample 1 was taken from a mechanical spindle of a precision machine tool. It belongs to an angular contact ball bearing (modeled as 7014), and the inner and outer diameters are 70 mm and 110 mm, respectively. The rotation speed is 8000–9000 rpm (heavy cut, in 30% operation time), and 10,000–11,000 rpm (finish machining, in 50% operation time). The total operation time is ~4500 h. Sample 2 was taken from the spindle of the motor, which is a deep groove ball bearing (modeled as 6316), and the inner and outer diameters are 80 mm and 170 mm, respectively. The operation parameters in Sample 2 cannot be confirmed. The contact stresses are affected by cargo weight (motor power). The two samples are both steel ball bearings, and the steel balls and raceways were all made of typical GCr15 (AISI 52100) martensite-bearing steel. The chemical component of the inner rings of each sample and reference ranges are listed in Table 1. The results show that the two samples both fall in the scope of normal chemical components of GCr15. The components of the C and Cr elements are both ~1 wt% and ~1.5 wt%, respectively. The microstructure is cryptocrystalline martensite, and the main phases are martensite, carbide particles, and retained austenite [37].

Table 1. The chemical component (wt%) of the inner rings of each sample.

Elements	C	Si	Mn	Cr	Mo	P	S	Ni	Cu
Reference Ranges	0.95~1.05	0.15~0.35	0.25~0.45	1.40~1.65	≤0.10	≤0.025	≤0.02	≤0.25	≤0.25
Sample 1	0.98	0.31	0.41	1.56	<0.01	0.018	0.0041	0.05	0.06
Sample 2	0.95	0.30	0.40	1.64	0.0443	0.0126	0.0038	0.0056	0.0625

In this study, the inner ring raceways were mainly characterized and analyzed. The raceways of the samples were dissected along the axial direction and circumferential direction. The metallographic samples were ground and polished. The samples were etched with 4% nital solution to show the cross-section of the microstructure. The macroscopic damage characteristics of raceways were observed by a stereomicroscope (ZEISS Stemi 508, made in Germany). An optical microscope (ZEISS Axio Observer Z1m, made in Germany) was used to observe the metallograph. A scanning electron microscope (Philips XL30, made in The Netherlands) was employed to observe microscopic features, such as surface damage and the microstructure. An Electron Back Scatter Diffraction (EBSD, Symmetry S2, made in UK) is used to further detect the features of grains. The hardness distributions of the microstructure were tested by a Vickers micro-hardness testing system (LM-247AT, made in the USA).

3. Results

3.1. Surface Morphologies of the Two Bearing Samples

The surface damage morphologies of the bearing samples have been characterized by macro- and microaspects. The macromorphologies show the severe damage of the raceways (in Figure 1). The macroscopic cracks (pointed by yellow arrows) distribute at bilateral contact bands, which seems like a typical surface damage characteristic of bearings with the WEL and BEL on the surface. Additionally, material removal or peeling can also be found on raceways. Wan's results [9] also show bilateral cracks and severe material removal phenomena. On the contact surfaces of rails, there are some relationships between the WEL and surface squats [29]. In this study, the relationship between the WEL/BEL and crack propagation behaviors of bearing raceways will be discussed in Section 4.2.
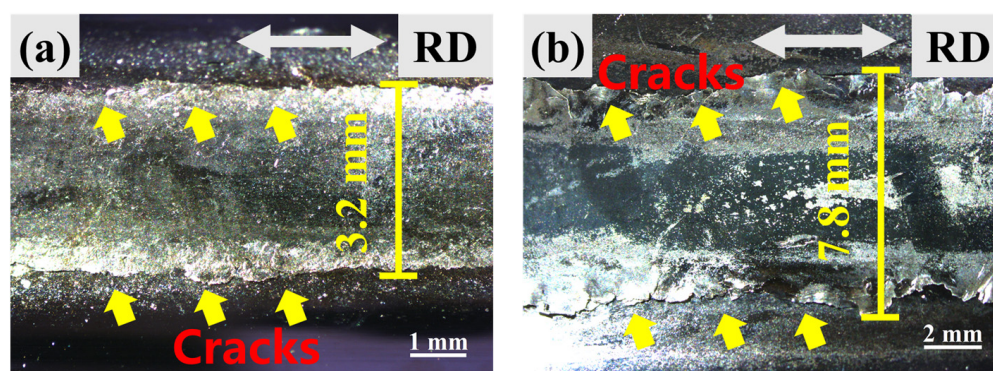

Figure 1. The macromorphologies of inner-ring raceway surfaces: (**a**) Sample 1 and (**b**) Sample 2. The cracks are pointed out by yellow arrows.

The micromorphologies of the raceway surface observed by SEM are shown in Figures 2 and 3. The high-magnification images of local areas in Figures 2a and 3a are shown in Figures 2b–e and 3b–e, respectively. The features of damaged raceways are significantly different in these local areas, but there are some common damage features between the two samples. Fish scale cracks (in Figures 2b and 3b) correspond to the macroscopic cracks in Figure 1, which shows that surface material has detached from surfaces gradually. At the roots of fish scale cracks, plastic deformation can be observed (in Figures 2c and 3c), indicating that the cracks may propagate or fracture in these regions. Surface peelings (in Figures 2d and 3d) and micropits (in Figures 2e and 3e) also distribute on the raceways, which belong to the typical surface rolling contact fatigue (RCF) behaviors on bearing raceways [38–41]. The surface damage (peelings or micropits) is one of the reasons for the increasing vibration values of these bearings.

3.2. Section Microstructure of the Two Bearing Samples (Optical Microscope)

The circumferential and axial cross-section microstructure images of the two samples are observed by an optical microscope (in Figures 4 and 5). Corresponding hardness distributions are shown in Figure 6. The matrix of these bearing samples is typical GCr15 (AISI 52100) martensite-bearing steel, and the general hard values are both ~720 HV. A schematic (Figure 7) shows the differences in the structure of the surface layer of the two samples.

In Sample 1, the WEL and BEL both distribute on the upper layer of the raceway surface (in Figure 4a,b), forming a sandwich structure. Figure 4c–f show the high-magnification images in Figure 4a. Some large grains can be observed in the WEL (in Figure 4c), indicating the growth of grains in the WEL by some driving forces. A flow structure exists in the WEL (in Figure 4d), which means that the plastic deforms under contact stress. In the BEL (Figure 4e), the microstructure is cryptocrystalline martensite because these fine grains cannot be observed by an optical microscope. The hardness values of the WEL and BEL are 600–800 HV and 800–900 HV, respectively. The hardness of the BEL is obviously higher

than that of the WEL. Different from Figure 4a–e, Figure 4f shows the boundary of the BEL/matrix, which is etched by an aqueous solution of sodium metabisulfite (10 g $Na_2S_2O_5$ in 100 mL distilled water). The etching time was about 15 s, and oscillation was performed strongly during the whole etching time. In Figure 4f, the blue (or black) regions are fine bainite and the dark and light brown areas are martensite [42].
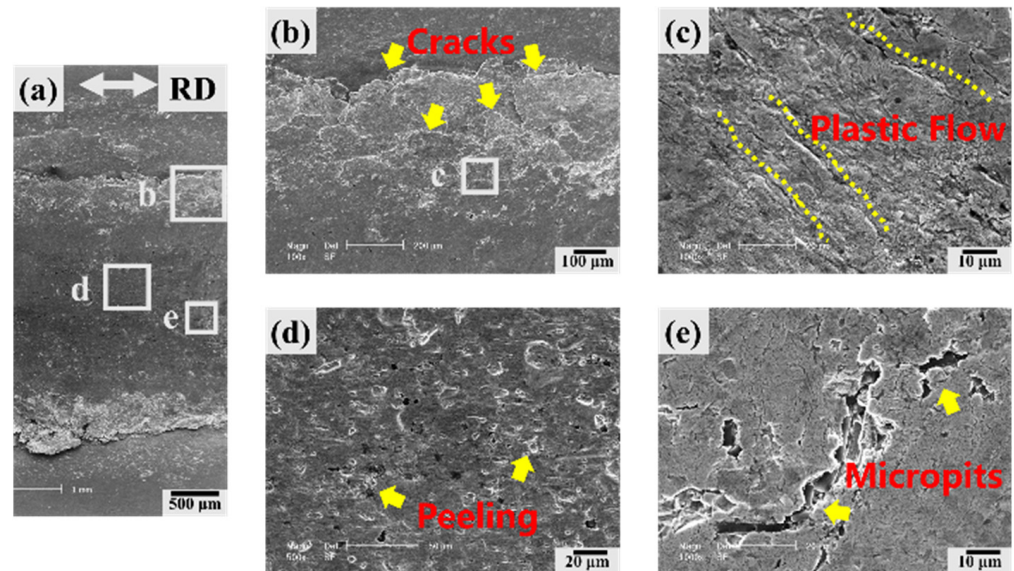

Figure 2. The micro-morphologies of inner-ring raceway surfaces of Sample 1. (**a**) The low magnification image of the raceway; (**b**–**e**) the high-magnification images of local areas in (**a**). Fish scale cracks, plastic flow, peeling, and micropits can be observed in (**b**–**e**), respectively.
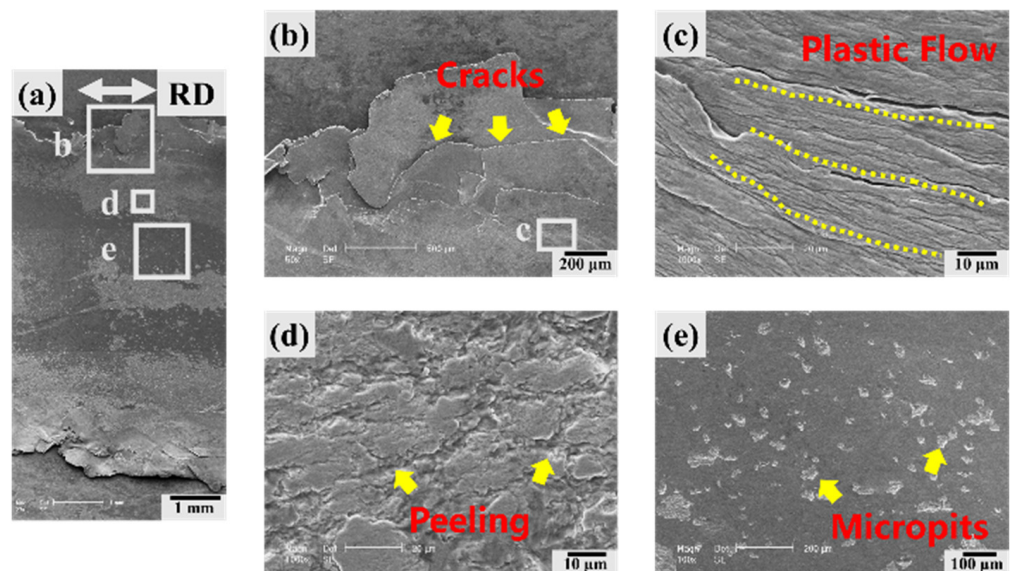

Figure 3. The micro-morphologies of inner-ring raceway surfaces of Sample 2. (**a**) The low magnification image of the raceway; (**b**–**e**) the high-magnification images of local areas in (**a**). Fish scale cracks, plastic flow, peeling, and micropits can be observed in (**b**–**e**), respectively.
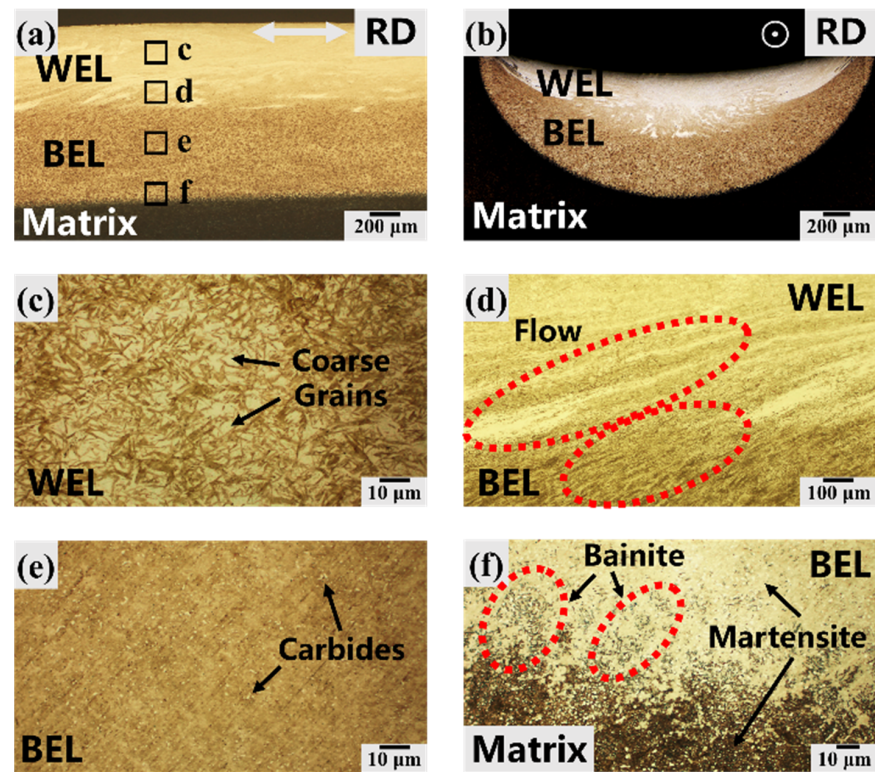
Figure 4. The cross-section microstructure (OM) of Sample 1: (**a**,**c**–**f**) circumferential; (**b**) axial. (**a**,**b**) The low magnification image of the upper layers; (**c**) the WEL; (**d**) flow microstructure; (**e**) the BEL; (**f**) bainite at the boundary of the BEL/matrix (etched by aqueous solution of sodium metabisulfite).
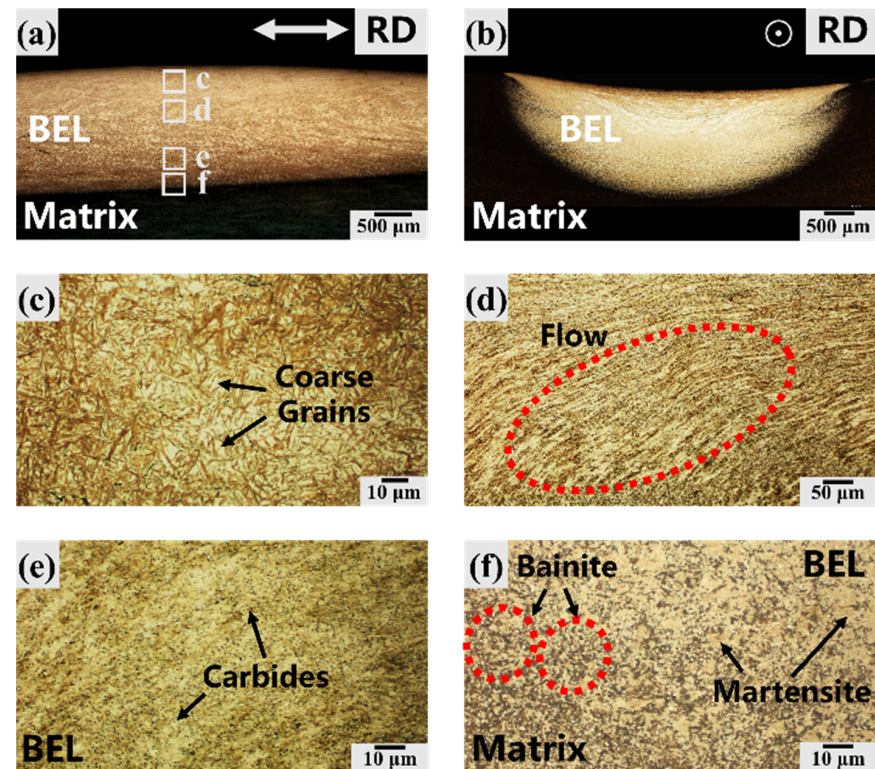

Figure 5. The cross-section microstructure (OM) of Sample 2: (**a**,**c**–**f**) circumferential; (**b**) axial. (**a**,**b**) The low magnification image of the upper layers; (**c**) coarse grains; (**d**) flow microstructure; (**e**) the BEL; (**f**) bainite at the boundary of the BEL/matrix (etched by aqueous solution of sodium metabisulfite).
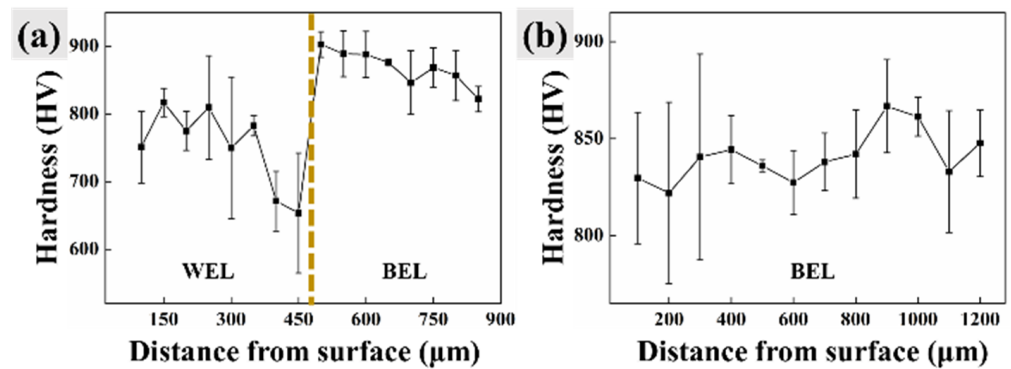
Figure 6. The hardness distributions of the surface layers. X-axis: the distance from the surface (μm); Y-axis: the hardness values (HV). (**a**) Sample 1; (**b**) Sample 2.
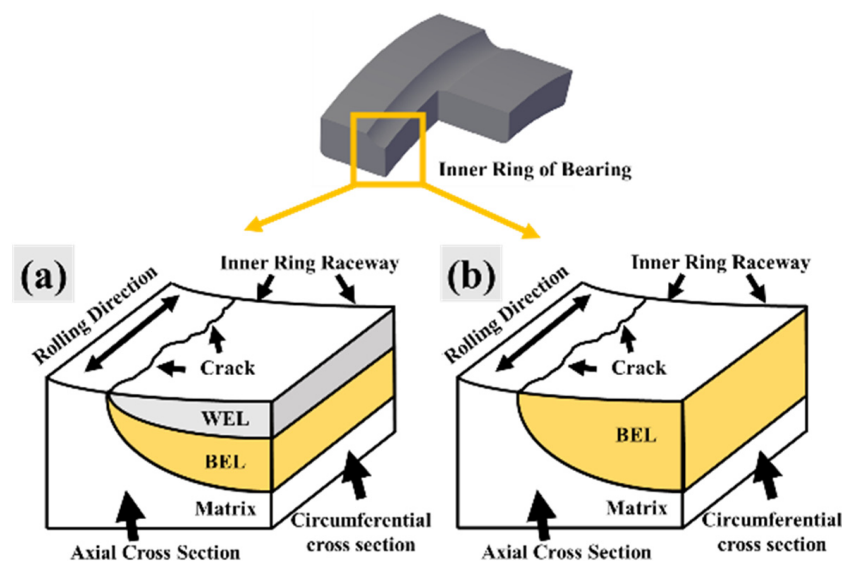

Figure 7. The structural schematics of surface layers of Sample 1 (**a**) and Sample 2 (**b**). The axial and circumferential cross-sections have been marked in the schematics. The BEL can be observed in two samples, but the WEL can be only seen in Sample 1.

In Sample 2, only the BEL can be seen in the cross-section images (in Figure 5a,b). Figure 4c–f show the high-magnification images in Figure 5a. Coarse grains and flow structure can also be observed from high-magnification images (as shown in Figure 5c,d). In Figure 5e, the BEL still consists of abundant cryptocrystalline martensite with hardness values 800–900 HV (apparently higher than that of the matrix). The hardness increase may also be caused by severe plastic deformation (work hardening effect), but the flow structure only appears in some local areas (in Figure 5d), which cannot explain the high hardness values of the entire BEL regions. Interestingly, on rail surfaces, the BEL cannot exist alone [1,14,43] and is generally located in the middle of the WEL and the matrix [7,8], which is opposite to the existence alone of the BEL in this study. However, the feature of high hardness values of the BEL on bearing raceways is similar to the WEL of railway surfaces. Figure 5f also shows the boundary of the BEL/matrix, which is etched by aqueous solution of sodium metabisulfite. The fine bainite and martensite can be seen simultaneously.

3.3. Section Microstructure and Crack Propagation Behavior of the Two Bearing Samples (Scanning Electron Microscope)

Figure 8 shows the microstructure and crack propagation (Sample 1) observed by SEM. Figure 8a–c show the images of the axial cross-section. Surface bilateral cracks initiate on the raceway surface (corresponding to the cracks in Figure 1) and then propagate downward.

According to the crack tips trend, cracks 1–3 will finally propagate upward until reaching the surface. Figure 8d–i show the microstructure from the near-surface layer to the matrix (circumferential cross-section). In Figure 8d, larger grains can be found in the WEL regions (corresponding to Figure 4c). Combined with the microstructure features and hardness distribution, the coarse grains (in Figure 8d–f) can be identified as austenite. Figure 8e,f show the elongated grains and flow microstructure in the WEL region (corresponding to Figure 4d). Plastic deformation occurs at this subsurface region because of the shear contact stress. The microstructure images of the BEL and the matrix are shown in Figure 8g,i, respectively. Spherical carbides can both be observed in the BEL and the matrix. The matrix can be regarded as the initial microstructure, i.e., the normal microstructure of GCr15 steel. The GCr15 matrix mainly contains abundant acicular martensite grains and sphere carbides. Plastic deformation can be barely found in the BEL and the matrix. Combined with the higher hardness values, it can be identified that the BEL mainly contains quenched martensite. The carbide element separating from supersaturated solid solution is the main difference between quenched martensite and tempered martensite [44]. Owing to the precipitation of ε-carbides, the tempered martensite can be easily etched by nital. Figure 8h is the boundary of the BEL and the matrix. According to the metallograph (Figure 4f), it can be known that bainite exists in this region. The phase transformation of bainite depends on the cooling rate to some extent [45].
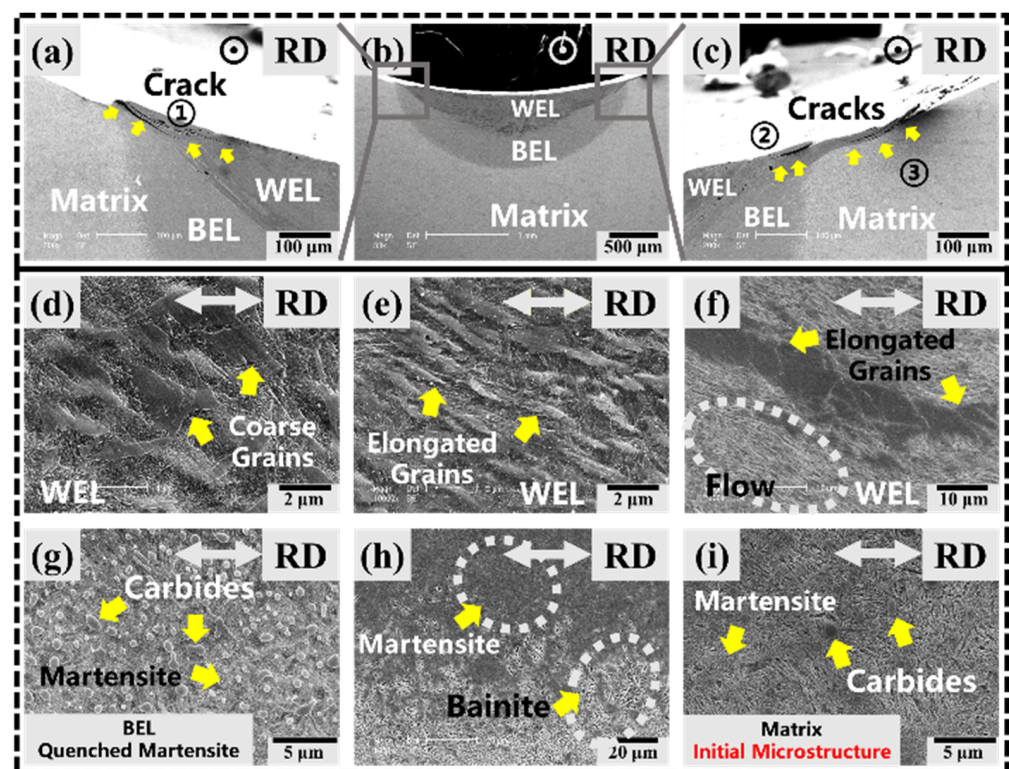

Figure 8. The microstructure (Sample 1) observed by SEM. (**a**–**c**) Bilateral cracks of the WEL/BEL/matrix (axial cross-section); (**d**–**i**) microstructure from the upper layer to the matrix (circumferential cross-section); (**d**) coarse grains in the WEL; (**e**) elongated grains; (**f**) flow microstructure; (**g**) quenched martensite in the BEL; (**h**) bainite at the boundary of the BEL/matrix; (**i**) the matrix near initial microstructure (GCr15).

The microstructure and crack propagation (Sample 2) observed by SEM is shown in Figure 9. Figure 9a,c show the axial cross-sections of surface bilateral cracks. According to the propagate direction of cracks tips, cracks 4 and 5 will propagate downwards to a certain depth and then continually propagate upward until reaching the surface, resulting in the surface peeling being much deeper (exceeding 100 μm) than that of Sample 1. Surface crack

propagation behaviors of the two bearings should be closely linked with the microstructure of the WEL/BEL. Microstructures from the near-surface layer to the matrix (circumferential cross-section) are shown in Figure 9d–i. Coarse grains can be found in Figure 9d, indicating that austenitizing was occurring in this region. Elongated coarse grains are found in Figure 9e, which corresponds to the metallographs in Figure 5d. Figure 9f shows a spherical cementite dissolving, indicating that the dissolution–diffusion–redistribution of carbon element occurs in the process of austenitizing. Figure 9g–i show the areas located below the flow structure. Similar to the results in Figure 8g–i, the BEL (quenched martensite) and the matrix (tempered martensite) can also be identified in Figure 9g,i, respectively. Figure 9h shows that this easily etched microstructure is bainite at the boundary of the BEL and the matrix [45,46].
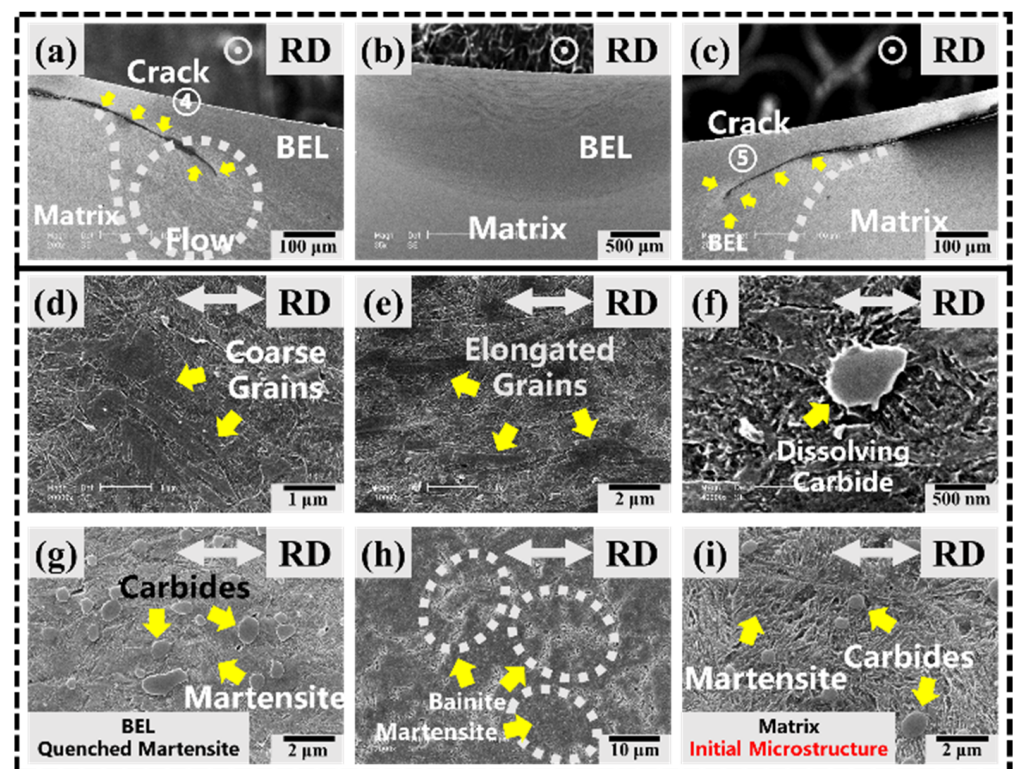

Figure 9. The microstructure (Sample 2) observed by SEM. (**a**–**c**) Bilateral cracks of the BEL/matrix (axial cross-section); (**d**–**i**) microstructure from the upper layer to the matrix (circumferential cross-section); (**d**) coarse grains; (**e**) elongated grains; (**f**) a dissolving carbide; (**g**) quenched martensite in the BEL; (**h**) bainite at the boundary of the BEL/matrix; (**i**) the matrix near initial microstructure (GCr15).

Figure 10 shows the EBSD results of the WEL and BEL from Sample 1 (corresponding to Figure 8d,g). Figure 11 shows the EBSD results of the near-surface regions and away from the surface in Sample 2 (corresponding to Figure 9d,g). Figure 12 are the high-magnification images in Figures 10 and 11. It can be seen that the samples all mainly contain austenite (yellow phase), martensite (red phase), and carbides (blue phase). According to the EBSD results of the WEL in Sample 1, the content of austenite exceeds 20%, and the content of martensite is ~70.4%. Nevertheless, the BEL consists of austenite (only 4.96%), and the content of martensite is ~83%. These results indicate that the phase transformation from martensite to austenite had occurred in the WEL regions. Owing to the more austenite in the WEL, the hardness values of the WEL are lower than the BEL. In Sample 2, the EBSD results show that the content of austenite in the near-surface region (8.96%) is higher than that of regions away from the surface (0.73%). But, the content of martensite in the near-surface region (85%) is lower than that of regions away from the surface (90.7%). These results indicate that austenitizing was occurring in the near-surface regions, which

is also the reason for the longer error bars of hardness values in Figure 6b. The coarse martensite grains (②) and ⑤) in Figure 12 also indicate the growth of martensite grains in these regions. In Figure 12, lower KAM values in coarse martensite grains (②) and ⑤) and coarse austenite grains (③ and ⑥) can be seen, as well as the higher KAM values in some fine martensite grains (①) and ④), which indicates the disappearance of lattice deformation in the processes of grain growth and phase transformation.
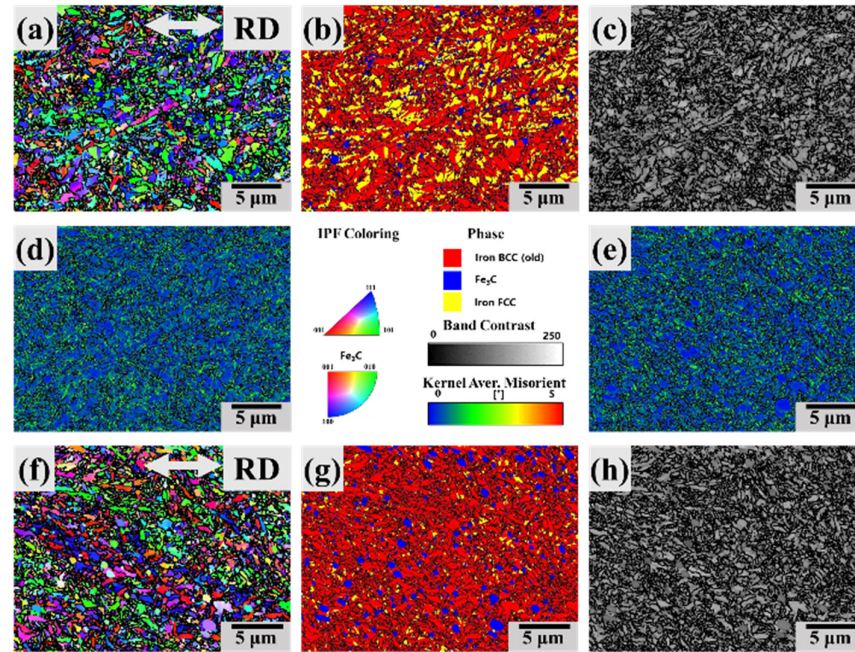

Figure 10. The EBSD microstructure of Sample 1 ((**a**–**d**) the WEL, corresponding to Figure 8d) and ((**e**–**h**) the BEL, corresponding to Figure 8g): (**a**,**f**) IPF map; (**b**,**g**) phase map; (**c**,**h**) BC map; (**d**,**e**) KAM map.
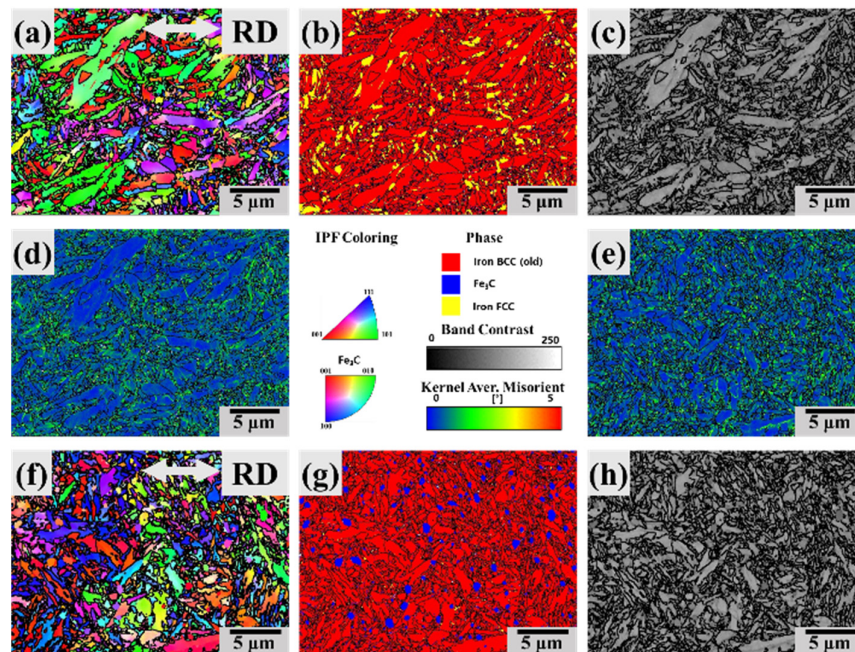

Figure 11. The EBSD microstructure of Sample 2 ((**a**–**d**) the near-surface region, corresponding to Figure 9d) and ((**e**–**h**) the region away from the surface, corresponding to Figure 9g): (**a**,**f**) IPF map; (**b**,**g**) phase map; (**c**,**h**) BC map; (**d**,**e**) KAM map.
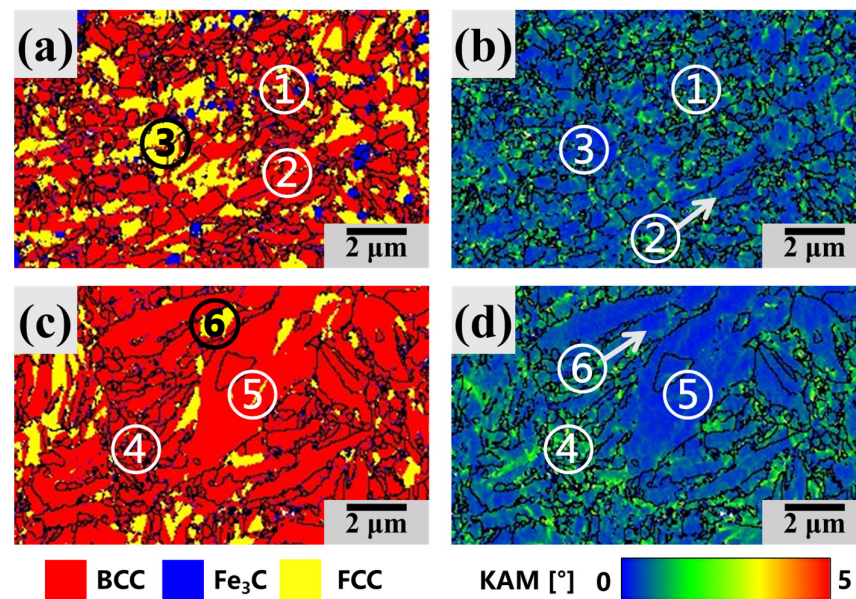
Figure 12. The high-magnification images of Figures 10 and 11: Sample 1 ((**a**,**b**) the WEL) and Sample 2 ((**c**,**d**) the near-surface region): (**a**,**c**) phase map; (**b**,**d**) KAM map.

4. Discussion

4.1. The Formation Mechanisms of the WEL and BEL on Martensite-Bearing Raceways

The BEL can be found on the raceways of the two samples, whereas the WEL can only be found in Sample 1, which means that the BEL and WEL may originate from two different processes. The main important differences between thermal-induced and stress-induced martensite are fine martensite grains in stress-induced martensite and severe plastic deformation in the boundary regions of the matrix [9,29,47]. In SEM images (Figures 8h and 9h), plastic deformation cannot be found in the boundary regions. Though some deformed grains can be found in Figure 8e,f and Figure 9e, they correspond to the local areas in Figures 4 and 5, which do not affect the formation mechanisms of the entire BEL. Thus, the thermal-induced effect is the main formation mechanism of the BEL. Owing to the surface relative roll and slip for a long time, the temperature of the contact surface is higher than austenite transformation points (A3 temperature), and then rapid cooling leads to the formation of quenched martensite, i.e., phase transformation. Another important feature of the thermal-induced effect is a sharp transition region at the boundary of the BEL/matrix [47,48]. Owing to the gradient distribution of temperature in the cross-section, austenite cannot form when the temperature is lower than the A3 temperature. The bainite found at the boundaries of the BEL and the matrix (shown in Figures 8h and 9h) also proves the phase transformation results from the thermal-induced effect. The different cooling rates result in this region transforming to bainite (temperature decreases slowly in this region). However, these bainite regions cannot be found at the boundaries of the WEL/matrix on pearlite railway surfaces [19,29,49], which may be associated with the higher cooling rate of the whole region. Messaadi [8] found the BEL layer from the upper layer of the rail surface, which had been identified as granular bainite, and also pointed out that the difference in the cooling rate between surface and subsurface regions is the reason for bainite phases.

The WEL can only be found in Sample 1. Compared with the BEL, the lower hardness of the WEL and coarse grains (in Figure 8d,e) prove an austenitizing process in this region. The EBSD results in Figure 10b,g also prove this phase transformation. Based on the thermal-induced effect, Zhang [11] speculated two formation mechanisms of the WEL: one is the WEL and BEL form simultaneously owing to surface uneven heat diffusion, and the other is the surface temperature increase (exceeding the A3 point) again, and then holding and slow cooling occur in these regions, leading to austenitizing and grain growth. The percentage

of austenite and hardness values depend on temperature and heat preservation time. Takahashi [3] pointed out that the surface quenched layer forms first, and then the hardness values of the surface layer decrease because the surface temperature increases again (under continuously cyclic contact), leading to high-temperature tempering of the surface layer. Plastic deformation can also be found in some local grains (in Figure 8e,f), which may be caused by shear stress. Thus, it can be speculated that the refinement and recrystallization of austenite grains occur under contact shear stress in the austenitizing process.

In Sample 2, similar elongated and coarse grains are shown in Figure 9d,e, indicating that austenitizing and plastic deformation were occurring in these regions. The wider error bars of hardness values (in Figure 6b) corresponding to the region from the topmost surface to ~400 μm below are obviously wider (the maximum and minimum hardness values are 900 HV and 750 HV, respectively), which also indicates the simultaneous existence of austenite and quenched martensite. The austenite and martensite phase also can be both identified by EDSD directly. Figure 9f also shows that a spherical carbide was dissolving, confirming the process of the dissolution–diffusion–redistribution of carbon in this region. Carbide particles can dissolve under the stress effect or the thermal effect. However, Qin [21] studied the carbide decomposition in GCr15 steel during high-pressure torsion and pointed out that the unsharp boundary between the carbides and matrix is the feature of decomposition under stress effect. On the contrary, in this study, the clear boundary (in Figure 9f) means the thermal effect is the main reason for carbide dissolution.

4.2. The Crack Propagation Behavior in the Surface Stratification Microstructure

Due to the differences in hardness values and main phases, the cracks initiate easily at boundaries between two types of different layers [29,35,50,51], such as the WEL/BEL, the WEL/matrix, or the BEL/matrix. As shown in Figure 8a,c (Sample 1) and Figure 9a,c (Sample 2), cracks 1–2 initiate at the boundary of the WEL and BEL and cracks 3–5 initiate at the boundary of the BEL and the matrix. There are some similar features of fracture modes of the cracks in the two samples. As Ren [36] pointed out, fracture modes I, II, and III dominate the propagation behaviors of fatigue cracks independently and synergistically in different propagation stages. Owing to the relative roll and slip of the balls, when the loads near the surface crack, the cracks are mainly affected by the shear stress, and the fracture mode is mainly II; when the loads pass directly above the surface cracks, modes I, II, and III dominate the propagation behaviors synergistically. However, crack propagation behaviors are also affected by hardness values and the microstructure of different layers, leading the different propagated paths. The schematics of crack propagation behaviors are shown in Figure 13.
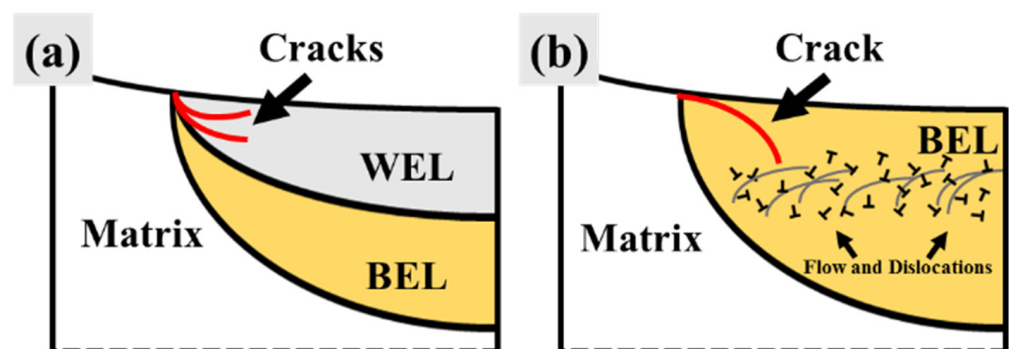

Figure 13. The axial cross-section schematic of crack propagation behaviors of Sample 1 (**a**) and Sample 2 (**b**). The cracks are marked in red lines.

In Sample 1, cracks 1–3 propagate along roughly the boundaries of the WEL/BEL/ matrix. Because the hardness values of the WEL are lower than the BEL, it is difficult for the cracks to propagate from the WEL to the BEL without a higher driving force. When the cracks propagate along the boundary to some extent, the crack tips turn upward until

reaching the surface (shown in Figure 13a). The maximum depth of the cracks is ~10 μm, and peeling bands are shallower. In Sample 2, because the BEL mainly consists of quenched martensite with hardness values of ~830 HV, the cracks can propagate easily in brittle structures. Thus, the maximum depth of the cracks (cracks 4 and 5 shown in Figure 9a,c) exceeds 100 μm, and it may further increase. It should be noted that crack 4 gradually propagates into flow regions, but the dense dislocations pileups originating from plastic deformation can hinder further crack propagation. In the stress-induced WEL from pearlite rails, Carroll [36] pointed out that the cracks within the WEL hardly propagate vertically. This is because the pearlite and deformed structures contain lamellar structures. Thus, the cracks turn and tend to propagate parallel to the WEL. Also, cracks 4 and 5 hardly cross the deformed matrix because of the working hardening effect in flow regions. Meanwhile, the crack growth is affected significantly by the stress field. The Hertz contact stress decreases gradually at the region exceeding 100 μm below the surface. Thus, crack propagation may be further hindered. Additionally, combined with the EBSD results, coarse austenite and martensite in the surface layer can also be found. The cracks might be affected by the brittleness or toughness of different microstructure. In the WEL in Sample 1, the content of austenite significantly increases (exceeding 20%). The cracks can be hindered by the tough austenite grains. However, in Sample 2, the brittle martensite grains can promote crack propagation. Furthermore more, the coarsening martensite and the decrease in grain boundaries lead to the hindering effect of cracks, which decreases significantly. Thus, the cracks can propagate deeper.

5. Conclusions

In this study, the WEL and BEL are found on two bearing samples. Their features have been characterized by OM and SEM et al. This study aims at further understanding the WEL and BEL and the crack propagation behaviors on martensite-bearing raceways. According to the discussion in this study, several conclusions have been listed as follows.

1. The BEL mainly consists of quenched martensite with hardness values of 800–900 HV. The thermal-induced effect is the main formation mechanism. Surface temperature first exceeds the A3 point during operation, and then rapidly cools, which leads to the austenitizing of the matrix and the transformation into quenched martensite. The bainite exists at the boundary of the BEL/matrix, and formation of the bainite originates from the slower cooling rate compared with that of the BEL regions.

2. It can be speculated that the WEL form after the BEL. The surface temperature increases again, leading to the surface austenitizing or high-temperature tempering. Austenite can retain room temperature due to slow cooling along with the occurrence of dissolution–diffusion–redistribution of carbon in this region. The coarse and deformed austenite grains indicate that the refinement and growth of grains occur in the austenitizing process.

3. Bilateral cracks may be the typical features of raceway surfaces with the WEL and BEL. The cracks can initiate at the boundaries of the WEL/BEL/matrix. The crack propagation behaviors are significantly affected by the mechanical properties of the WEL and BEL. They can hardly propagate from a softer WEL to a harder BEL. Thus, cracks in the WEL regions are shallower.

4. Because the BEL mainly consists of brittle quenched martensite, the cracks can easily propagate downward. Thus, the depth of cracks in the BEL can exceed 100 μm. The plastic deformation and gradually decreasing contact stress in the subsurface region can simultaneously hinder crack propagation.

Author Contributions: X.Z.: Investigation, experiment, methodology, and writing; D.W. and J.W.: Supervision, methodology, and revision; Y.Z.: Methodology and experiment; L.X. and E.-H.H.: Investigation. All authors have read and agreed to the published version of the manuscript.

References

1. Nguyen, B.H.; Al-Juboori, A.; Zhu, H.T.; Zhu, Q.; Li, H.J.; Tieu, K. Formation mechanism and evolution of white etching layers on different rail grades. *Int. J. Fatigue* **2022**, *163*, 107100. [CrossRef]
2. Al-Juboor, A.; Zhu, H.; Wexler, D.; Li, H.; Lu, C.; McCusker, A.; McLeod, J.; Pannila, S.; Barnes, J. Characterisation of White Etching Layers formed on rails subjected to different traffic conditions. *Wear* **2019**, *436–437*, 202998. [CrossRef]
3. Takahashi, J.; Kawakami, K.; Ueda, M. Atom probe tomography analysis of the white etching layer in a rail track surface. *Acta Mater.* **2010**, *58*, 3602–3612. [CrossRef]
4. Mojumder, S.; Mishra, K.; Singh, K.; Qiu, C.; Mutton, P.; Singh, A. Effect of track curvature on the microstructure evolution and cracking in the longitudinal section of lower gauge corner flow lips formed in rails. *Eng. Fail. Anal.* **2022**, *135*, 106117. [CrossRef]
5. Nguyen, B.H.; Al-Juboori, A.; Zhu, H.T.; Gazder, A.A.; Li, H.J.; Tieu, K. Fracture mechanisms in rails with mechanically and thermomechanically-induced white etching layers under three-point bending. *Eng. Fail. Anal.* **2022**, *131*, 105813. [CrossRef]
6. Li, S.G.; Wu, J.; Petrov, R.H.; Li, Z.; Dollevoet, R.; Sietsma, J. "Brown etching layer": A possible new insight into the crack initiation of rolling contact fatigue in rail steels? *Eng. Fail. Anal.* **2016**, *66*, 8–18. [CrossRef]
7. Kumar, A.; Agarwal, G.; Petrov, R.; Goto, S.; Sietsma, J.; Herbig, M. Microstructural evolution of white and brown etching layers in pearlitic rail steels. *Acta Mater.* **2019**, *171*, 48–64. [CrossRef]
8. Messaadi, M.; Steenbergen, M. Stratified surface layers on rails. *Wear* **2018**, *414–415*, 151–162. [CrossRef]
9. Wan, L.B.; Li, S.X.; Lu, S.Y.; Su, Y.S.; Shu, X.D.; Huang, H.B. Case study: Formation of white etching layers in a failed rolling element bearing race. *Wear* **2018**, *396–397*, 126–134. [CrossRef]
10. Guzmán, F.G.; Sous, C.; Van, L.H.; Jacobs, G. An energetic approach for the prognosis of thermally induced white etching layers in bearing steel 100CrMn6. *Tribol. Int.* **2020**, *143*, 106096. [CrossRef]
11. Zhang, X.C.; Wu, D.; Xia, Z.F.; Zhang, Y.M.; Li, Y.F.; Wang, J.Q.; Han, E.H. Microstructure characteristics and formation mechanisms of white etching layer (WEL) and brown etching layer (BEL) on martensite bearing raceway. *J. Mater. Res. Technol.* **2023**, *25*, 4876–4887. [CrossRef]
12. Gao, G.H.; Liu, M.; Gui, X.L.; Hu, J.; Luan, J.H.; Jiao, Z.B.; Wang, X.; Bai, B.Z.; Yang, Z.G. Heterogenous structure and formation mechanism of white and brown etching layers in bainitic rail steel. *Acta Mater.* **2023**, *250*, 118887. [CrossRef]
13. Zhou, Y.; Mo, J.L.; Cai, Z.B.; Deng, C.G.; Peng, J.F.; Zhu, M.H. Third-body and crack behavior in white etching layer induced by sliding–rolling friction. *Tribol. Int.* **2019**, *140*, 105882. [CrossRef]
14. Lian, Q.L.; Deng, G.Y.; Zhu, H.T.; Li, H.J.; Wang, X.; Liu, Z.M. Influence of white etching layer on rolling contact behavior at wheel-rail interface. *Friction* **2020**, *8*, 1178–1196. [CrossRef]
15. Merino, P.; Cazottes, S.; Lafilé, V.; Risbet, M.; Saulot, A.; Bouvier, S.; Marteau, J.; Berthier, Y. An attempt to generate mechanical white etching layer on rail surface on a new rolling contact test bench. *Wear* **2021**, *482–483*, 203945. [CrossRef]
16. Baumann, G.; Fecht, H.J.; Liebelt, S. Formation of white-etching layers on rail treads. *Wear* **1996**, *191*, 133–140. [CrossRef]
17. Österle, W.; Rooch, H.; Pyzalla, A.; Wang, L. Investigation of white etching layers on rails by optical microscopy, electron microscopy, X-ray and synchrotron X-ray diffraction. *Mater. Sci. Eng. A* **2001**, *303*, 150–157. [CrossRef]
18. Wu, J.; Petrov, R.H.; Naeimi, M.; Li, Z.; Dollevoet, R.; Sietsma, J. Laboratory simulation of martensite formation of white etching layer in rail steel. *Int. J. Fatigue* **2016**, *91*, 11–20. [CrossRef]
19. Su, C.R.; Shi, L.B.; Wang, W.J.; Wang, D.Z.; Cai, Z.B.; Liu, Q.Y.; Zhou, Z.R. Investigation on the rolling wear and damage properties of laser dispersed quenched rail materials treated with different ratios. *Tribol. Int.* **2019**, *135*, 488–499. [CrossRef]
20. Wilches, P.L.V.; Wang, L.; Mellor, B.G.; Huang, Y. White etching structures in annealed 52100 bearing steel arising from high-pressure torsion tests. *Tribol. Int.* **2021**, *164*, 107187. [CrossRef]
21. Qin, Y.; Mayweg, D.; Tung, P.Y.; Pippan, R.; Herbig, M. Mechanism of cementite decomposition in 100Cr6 bearing steels during high pressure torsion. *Acta Mater.* **2020**, *201*, 79–93. [CrossRef]
22. Yang, Z.N.; Jiang, F.; Wang, Y.M.; Wang, Q.C.; Huang, M.X.; Wang, Y.F.; Chen, C.; Zhang, F.C. Making composite steel higher strength and higher ductility via introducing carbon diffusion strategy. *Mater. Res. Lett.* **2021**, *9*, 391–397. [CrossRef]
23. Wang, Y.L.; Chen, Y.L.; Yu, W. Effect of Cr/Mn segregation on pearlite—Martensite banded structure of high carbon bearing steel. *Int. J. Miner. Metall. Mater.* **2021**, *4*, 665–675. [CrossRef]
24. Elkot, M.N.; Sun, B.H.; Zhou, X.Y.; Ponge, D.; Raabe, D. On the formation and growth of grain boundary κ-carbides in austenitic high-Mn lightweight steels. *Mater. Res. Lett.* **2024**, *12*, 10–16. [CrossRef]
25. Li, Y.S.; Dong, Y.W.; Jiang, Z.H.; Tang, Q.F.; Du, S.Y.; Hou, Z.W. Influence of rare earth Ce on hot deformation behavior of as-cast Mn18Cr18N high nitrogen austenitic stainless steel. *Int. J. Miner. Metall. Mater.* **2023**, *30*, 324. [CrossRef]

26. Lojkowski, W.; Djahanbakhsh, M.; Bürkle, G.; Gierlotka, S.; Zielinski, W.; Fecht, H.J. Nanostructure formation on the surface of railway tracks. *Mater. Sci. Eng. A* **2001**, *303*, 197–208. [CrossRef]

27. Zhang, F.Y.; Duan, C.Z.; Wang, M.J.; Sun, W. White and dark layer formation mechanism in hard cutting of AISI52100 steel. *J. Manuf. Process.* **2018**, *32*, 878–887. [CrossRef]

28. Pal, S.; Daniel, W.J.T.; Farjoo, M. Early stages of rail squat formation and the role of a white etching layer. *Int. J. Fatigue* **2013**, *52*, 144–156. [CrossRef]

29. Al-Juboori, A.; Wexler, D.; Li, H.; Zhu, H.T.; Lu, C.; McCusker, A.; McLeod, J.G.; Pannil, S.; Wang, Z. Squat formation and the occurrence of two distinct classes of white etching layer on the surface of rail steel. *Int. J. Fatigue* **2017**, *104*, 52–60. [CrossRef]

30. Duan, C.; Qu, S.; Hu, X.; Jia, S.; Li, X. Evaluation of the influencing factors of combined surface modification on the rolling contact fatigue performance and crack growth of AISI 52100 steel. *Wear* **2022**, *494–495*, 204252. [CrossRef]

31. Wang, J.T.; Qu, S.G.; Lai, F.Q.; Hu, X.F.; Deng, Y.Q.; Li, X.Q. Synergistic effects of a combined surface modification technology on rolling contact fatigue behaviors of 20CrMoH steel under different contact stresses. *Int. J. Fatigue* **2021**, *153*, 106487. [CrossRef]

32. Gao, B.; Liu, Y.; Chen, X.J.; Han, Z.M.; Xu, X.Y.; Wang, Z.B. Effects of rare earth addition and service mode on surface integrity evolution of high-end machine tool spindle bearings under service. *J. Mater. Res. Technol* **2023**, *27*, 2814–2821. [CrossRef]

33. Ostash, O.P.; Anofriev, V.H.; Andreiko, I.M. On the concept of selection of steels for high-strength railroad wheels. *Mater. Sci.* **2013**, *48*, 697–703. [CrossRef]

34. Ren, Z.D.; Li, B.Z.; Zhou, Q.Z. Rolling contact fatigue crack propagation on contact surface and subsurface in mixed mode I + II + III fracture. *Wear* **2022**, *506–507*, 204459. [CrossRef]

35. Seo, J.; Kwon, S.; Jun, H.; Lee, D.H. Numerical stress analysis and rolling contact fatigue of White Etching Layer on rail steel. *Int. J. Fatigue* **2011**, *33*, 203–211. [CrossRef]

36. Carroll, R.I.; Beynon, J.H. Rolling contact fatigue of white etching layer: Part 1. *Wear* **2007**, *262*, 1253–1266. [CrossRef]

37. Wu, D.; Zhang, X.C.; Li, Y.F.; Wang, J.Q.; Han, E.H. Characterization of machined surface quality and near-surface microstructure of a high speed thrust angular contact ball bearing. *J. Mater. Sci. Technol.* **2021**, *86*, 219–226. [CrossRef]

38. Zhang, X.C.; Wu, D.; Xia, Z.F.; Li, Y.F.; Wang, J.Q.; Han, E.H. Study on surface fatigue and metamorphic layer of raceway of hybrid ceramic ball bearing in high-speed spindle for machine tool. *Eng. Fail. Anal.* **2023**, *143*, 106928. [CrossRef]

39. Zhang, X.C.; Wu, D.; Xia, Z.F.; Li, Y.F.; Wang, J.Q.; Han, E.H. Characteristics and mechanism of surface damage of hybrid ceramic ball bearings for high-precision machine tool. *Eng. Fail. Anal.* **2022**, *142*, 106784. [CrossRef]

40. Zhang, X.C.; Wu, D.; Xia, Z.F.; Li, Y.F.; Wang, J.Q.; Han, E.H. Comparative Study on Surface Contact Fatigue of Machine Tool Bearing Raceways with Different Rolling Elements: Two Failure Bearings Case Studies. *Tribol. Lett.* **2023**, *71*, 55–68. [CrossRef]

41. Mallipeddi, D.; Norell, M.; Naidu, V.M.S.; Zhang, X.; Näslund, M.; Nyborg, L. Micropitting and microstructural evolution during gear testing-from initial cycles to failure. *Tribol. Int.* **2021**, *156*, 106820. [CrossRef]

42. Zakerinia, H.; Kermanpur, A.; Najafizadeh, A. Color metallography; a suitable method for characterization of martensite and bainite in multiphase steels. *Inte. J. Iron. Steel. Society. Iran* **2009**, *6*, 14–18.

43. Steenbergen, M. Rolling contact fatigue: Spalling versus transverse fracture of rails. *Wear* **2017**, *380–381*, 96–105. [CrossRef]

44. Perez, M.; Sidoroff, C.; Vincent, A.; Esnouf, C. Microstructural evolution of martensitic 100Cr6 bearing steel during tempering: From thermoelectric power measurements to the prediction of dimensional changes. *Acta Mater.* **2009**, *57*, 3170–3181. [CrossRef]

45. Bhadeshia, H.K.D.H.; Honeycombe, R.W.K. *Steels: Microstructure and Properties*; Elsevier: London, UK, 2017.

46. Bhadeshia, H.K.D.H. *Bainite in Steels: Transformations, Microstructure and Properties*; IOM Communications: London, UK, 2001.

47. Zhou, Y.; Peng, J.F.; Luo, Z.P.; Cao, B.B.; Jin, X.S.; Zhu, M.H. Phase and microstructural evolution in white etching layer of a pearlitic steel during rolling-sliding friction. *Wear* **2016**, *362–363*, 8–17. [CrossRef]

48. Pal, S.; Daniel, W.J.T.; Valente, C.H.G.; Wilson, A.; Atrens, A. Surface damage on new AS60 rail caused by wheel slip. *Eng. Fail. Anal.* **2012**, *22*, 152–165. [CrossRef]

49. Pan, R.; Ren, R.; Chen, C.H.; Zhao, X.J. The microstructure analysis of white etching layer on treads of rails. *Eng. Fail. Anal.* **2017**, *82*, 39–46. [CrossRef]

50. Thiercelin, L.; Saint-Aimé, L.; Lebon, F.; Saulot, A. Thermomechanical modelling of the tribological surface transformations in the railroad network (white etching layer). *Mech. Mater.* **2020**, *151*, 103636. [CrossRef]

51. Rasmussen, C.J.; Fæster, S.; Dhar, S.; Quaade, J.V.; Manuel, B.; Danielsen, H.K. Surface crack formation on rails at grinding induced martensite white etching layers. *Wear* **2017**, *384–385*, 8–14. [CrossRef]